

---

# DIAGNOSING AND BREAKING AMPLITUDE SUPPRESSION IN SEISMIC PHASE PICKING THROUGH ADVERSARIAL SHAPE LEARNING

---

A PREPRINT

✉ **Chun-Ming Huang**

Department of Geosciences  
National Taiwan University  
Taipei, Taiwan  
jimmy60504@gmail.com

**Li-Heng Chang**

Department of Geosciences  
National Taiwan University  
Taipei, Taiwan  
qwert159784623@gmail.com

**I-Hsin Chang**

Department of Geosciences  
National Taiwan University  
Taipei, Taiwan  
atetgod000@gmail.com

✉ **An-Sheng Lee**

Marine Core Research Institute  
Kochi University  
Kochi, Japan  
aslee@kochi-u.ac.jp

✉ **Hao Kuo-Chen**

Department of Geosciences  
National Taiwan University  
Taipei, Taiwan  
kuochenhao@ntu.edu.tw

November 11, 2025

## ABSTRACT

Deep learning has revolutionized seismic phase picking, yet a paradox persists: high signal-to-noise S-wave predictions consistently fail to cross detection thresholds, oscillating at suppressed amplitudes. We identify this previously unexplained phenomenon as amplitude suppression, which we diagnose through analyzing training histories and loss landscapes. Three interacting factors emerge: S-wave onsets exhibit high temporal uncertainty relative to high-amplitude boundaries; CNN’s bias toward sharp amplitude changes anchors predictions to these boundaries rather than subtle onsets; and point-wise Binary Cross-Entropy (BCE) loss lacks lateral corrective forces, providing only vertical gradients that suppress amplitude while temporal gaps persist. This geometric trap points to a shape-then-align solution where stable geometric templates must precede temporal alignment. We implement this through a conditional GAN framework by augmenting conventional BCE training with a discriminator that enforces shape constraints. Training for 10,000 steps, this achieves a 64% increase in effective S-phase detections. Our framework autonomously discovers target geometry without a priori assumptions, offering a generalizable solution for segmentation tasks requiring precise alignment of subtle features near dominant structures.

**Keywords** Seismic Phase Picking · Generative Adversarial Networks · Geometric Loss Landscape · Training Bottleneck

## 1 Introduction

Seismic phase picking, the precise identification of seismic wave arrival times, is a fundamental task demanding extreme temporal accuracy. The advent of deep learning, particularly U-Net-based PhaseNet [Zhu and Beroza, 2018], revolutionized this field by representing discrete arrival times as truncated Gaussian probability distributions, effectively reframing the problem into one analogous to pinpointing a single pixel in image segmentation. This approach, however, reveals a striking paradox: for high signal-to-noise S-phases that should be easily identifiable, predicted probability peaks consistently fail to cross detection thresholds, remaining dynamically suppressed at intermediate amplitudes. This performance bottleneck, which we term amplitude suppression, manifests as an observable symptom whose underlying mechanism has remained unexplained. The typical response has been to refine architectures [Mousavi et al., 2020, Liao

et al., 2021], augment datasets [Li et al., 2024, Wang et al., 2021], or modify training objectives [Park and Beroza, 2025, Williams et al.], without diagnosing the underlying failure mechanism.

By analyzing training histories, we diagnose that suppression emerges as a dynamic process driven by three interacting factors: S-wave onsets exhibit high temporal uncertainty relative to subsequent high-amplitude boundaries, with their separation varying systematically with epicentral distance; CNN’s correlation-based mechanism anchors predictions on sharp amplitude changes rather than subtle onsets; and pointwise Binary Cross-Entropy (BCE) loss lacks lateral corrective forces to resolve temporal misalignment. Visualizing the theoretical loss landscape confirms this: pointwise BCE generates only vertical gradients that suppress amplitude when predictions deviate from the label center, while the temporal gap persists. This geometric trap points to a shape-then-align solution where stable geometric templates must precede temporal alignment, as shape deformation gradients would otherwise overwhelm the subtle signals needed for temporal fine-tuning.

We validated this by constraining model outputs to perfect Gaussian templates and observing the emergence of a single global minimum with strong lateral guidance. To realize this, we introduce a conditional GAN framework [Mirza and Osindero, 2014] inspired by pix2pix [Isola et al., 2016], conceptualizing seismic phase picking as translating waveforms into Gaussian-styled probability curves. Building upon conventional supervised training with BCE loss, we augment the framework with only a single additional component: the SeisBlue Discriminator (BlueDisc), an adaptive shape critic that enforces geometric coherence through adversarial learning. This minimal modification achieves a 64% increase in effective S-phase detections.

Our dual contribution lies in both diagnosis and solution: the theoretical analysis pinpoints how temporal uncertainty traps pointwise optimization, while the framework’s strength lies in its generality, autonomously discovering target geometry without a priori assumptions. This offers a new perspective for tackling similar geometric fitting challenges in higher dimensions.

## 2 Results

### 2.1 Observation of Amplitude Suppression

To investigate the root cause of amplitude suppression, we first examined training histories on individual seismic records. The training history of the conventional PhaseNet model [Zhu and Beroza, 2018] on a representative event reveals a complex and divergent dynamic process for P- and S-waves (Fig. 1). Initially, both predictions evolve similarly, forming a half-peak platform. However, a clear divergence occurs after the model begins to separate their features: while the P-phase prediction successfully grows in amplitude, the S-phase’s development is arrested as it approaches an amplitude of approximately 0.5, ultimately trapped in amplitude suppression.

This suppression manifests as two distinct symptoms in the final prediction for a waveform where the labeled onset is clearly separated from the subsequent high-amplitude wave packet (Fig. 2a, b). First, the probability peak is suppressed at an amplitude of approximately 0.5, well below the 0.7 detection threshold. Second, its location is systematically displaced toward the later, high-amplitude boundary. A large-scale statistical analysis of the entire test set (Fig. 3a) confirms that a dense cluster of S-phase predictions hovers in a horizontal band around the 0.5 amplitude level. Crucially, while many of these predictions are temporally accurate (within  $\pm 0.1$ s of the label), their insufficient peak height renders them ineffective, establishing suppression as a primary cause of detection failure.

### 2.2 Geometric Diagnosis of the Optimization Trap

We examined the geometric properties of the conventional training objective to understand the origin of this failure. A magnified view of a suppressed S-phase prediction (Fig. 4a) reveals its characteristic flattened-top appearance. We visualized the theoretical loss landscape of the point-wise BCE loss (Fig. 4b) to trace the source of this geometry. The visualization reveals the geometric origin of the trap: the landscape shows a low-loss region at the label peak, but this is a non-global minimum due to additional low-loss regions on both sides when amplitude is near zero. The point-wise BCE provides only vertical gradients without lateral guidance to resolve temporal misalignment.

To deconstruct the factors giving rise to this trap, we designed a numerical simulation that isolates its core mechanisms (Fig. 5). Crucially, we removed the entire neural network, leaving only trainable prediction values that are directly optimized by gradient descent. This stripped-down setup reveals a complex interplay between temporal uncertainty and systematic bias. High temporal uncertainty alone induces amplitude suppression (Fig. 5, top row); as the target distribution widens, the optimizer repeatedly enters and exits the label’s core region, preventing amplitude from growing consistently. Systematic bias causes significant temporal offset only when combined with high temporal uncertainty (Fig. 5, bottom row). When uncertainty is low, the optimizer achieves high amplitude despite the bias. In contrast, the

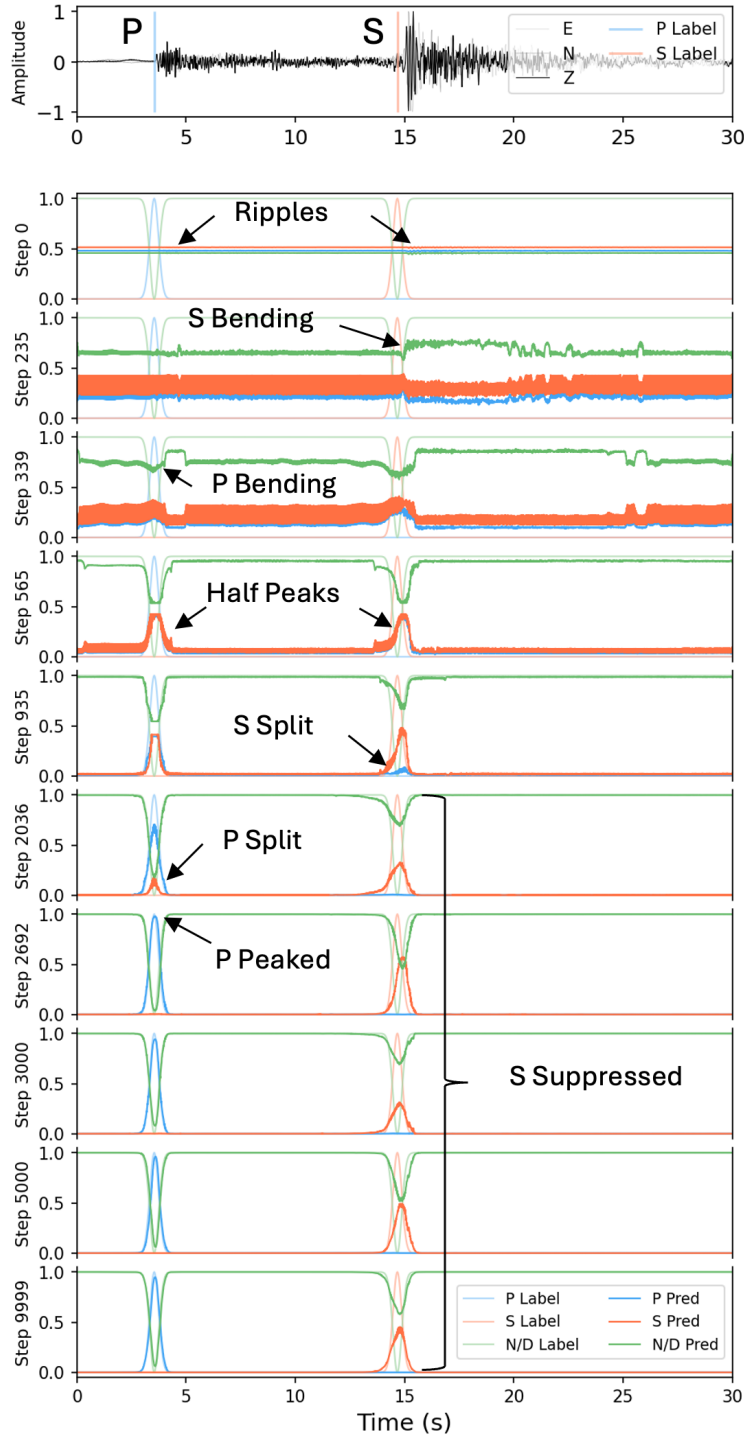


Figure 1: **The dynamic process of amplitude suppression.** Color coding: P-wave (blue), S-wave (orange), Noise (green); light/dark colors show labels/predictions. This figure visualizes key training steps from a conventional supervised model. The model exhibits a specific learning sequence: initially producing right-flanked responses at regions of sharpest amplitude change, then learning left flanks to form half-Gaussian curves with plateaus, and finally attempting to differentiate P/S features and grow peak amplitudes. However, even in late training stages, the S-phase peak remains trapped at  $\sim 0.5$  amplitude, oscillating in this suboptimal state. This depicts suppression as a dynamic process, not a static outcome. See Supplementary Movie 1 (10,000 steps) and Movie 2 (100,000 steps) for extended dynamics.

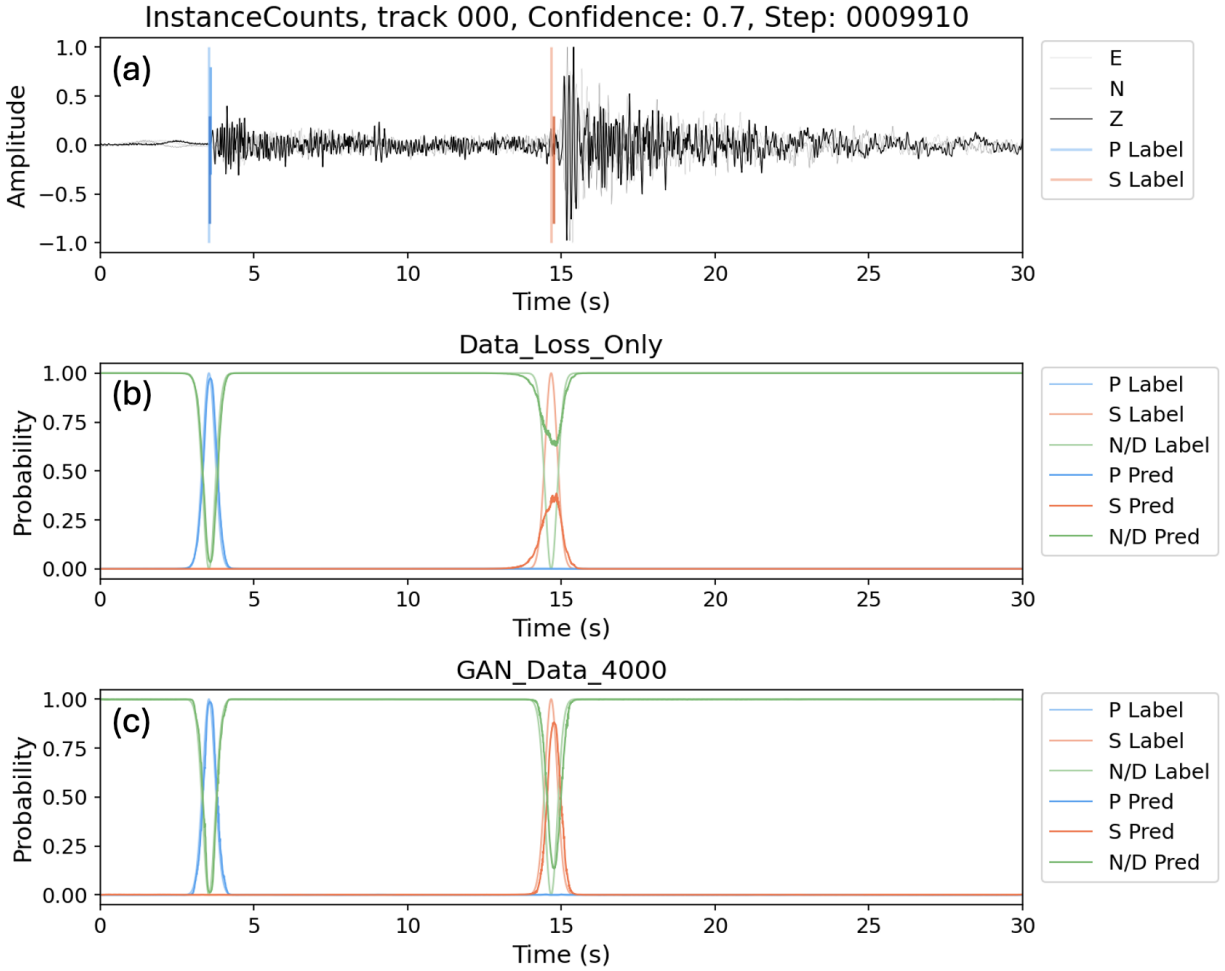
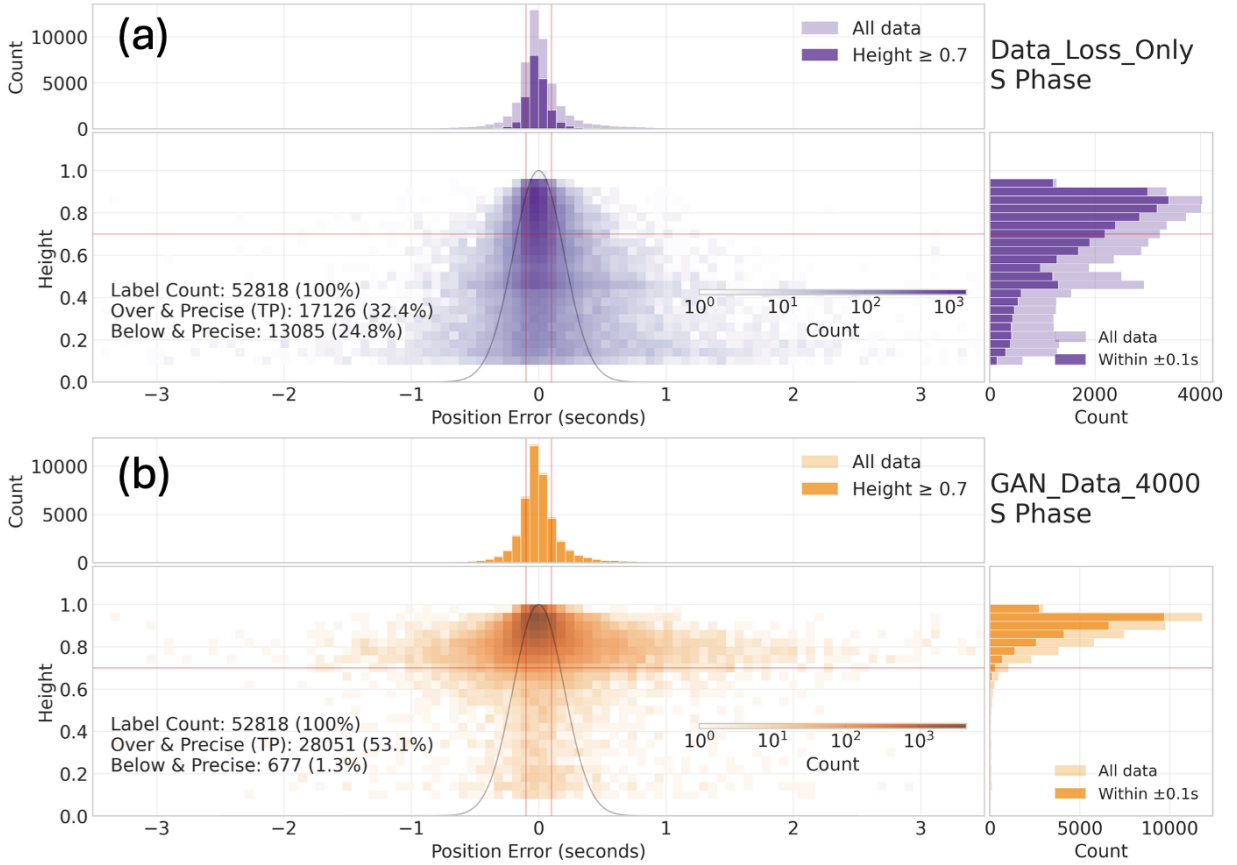


Figure 2: **Visual diagnosis and correction of amplitude suppression.** Color coding: P-wave (blue), S-wave (orange), Noise (green); light/dark colors show labels/predictions. (a) Representative waveform with phase arrival markers: longest line (reference label), upper short line (conventional prediction, panel b), lower short line (our framework, panel c). Note temporal delay between S-wave onset and high-amplitude wave packet. (b) Conventional method exhibits two suppression symptoms: peak amplitude suppressed at 0.5 (below 0.7 threshold) and temporal position shifted rightward toward high-amplitude boundary. (c) Our framework overcomes suppression: peak exceeds 0.7 threshold and temporal position calibrated within  $\pm 0.1$  s accuracy. See Supplementary Movie 1 (10,000 steps) and Movie 2 (100,000 steps) for complete training dynamics.



**Figure 3: Large-scale quantitative statistics of S-phase predictions: Confirmation and mitigation of suppression.** Black Gaussian curves represent reference labels (see Supplementary Fig. 6 for complete P- and S-wave comparison). (a) Conventional method: dense horizontal suppression band at 0.5 amplitude confirms widespread amplitude suppression. Many predictions within this band are temporally accurate ( $\pm 0.1$  s red lines) but ineffective due to insufficient amplitude. (b) Our framework: suppression band entirely eliminated, replaced by elliptical distribution centered on label apex. This elevates previously sub-threshold accurate predictions into detectable range, achieving 64% increase in effective S-phase detections (peak  $> 0.7$ , time error  $< 0.1$  s).

optimizer with a holistic Gaussian constraint remains robustly anchored near the distribution’s true center across all conditions, maintaining an amplitude of at least 0.5. This simulation deconstructs the two symptoms of suppression, attributing amplitude suppression primarily to temporal uncertainty and temporal offset to the convergence of both uncertainty and bias.

### 2.3 Conceptual Validation of the Decoupling Strategy

Having diagnosed the trap, we tested our core conceptual solution: decoupling shape learning from temporal localization. We visualized the loss landscape where the model could only output a perfect Gaussian template, calculating its holistic BCE loss as its peak moved across the amplitude-time plane (Fig. 4c). The resulting surface reveals a single, well-defined global minimum at the correct time and full amplitude, providing the strong lateral guidance absent in point-wise optimization. Our numerical simulation (Fig. 5) confirms this prediction: constraining the optimizer to Gaussian-shaped predictions maintains substantially higher peak amplitudes while anchoring predictions at the center of temporally uncertain targets, preventing the drift observed in point-wise optimization. This validates our decoupling strategy and guides our cGAN implementation.

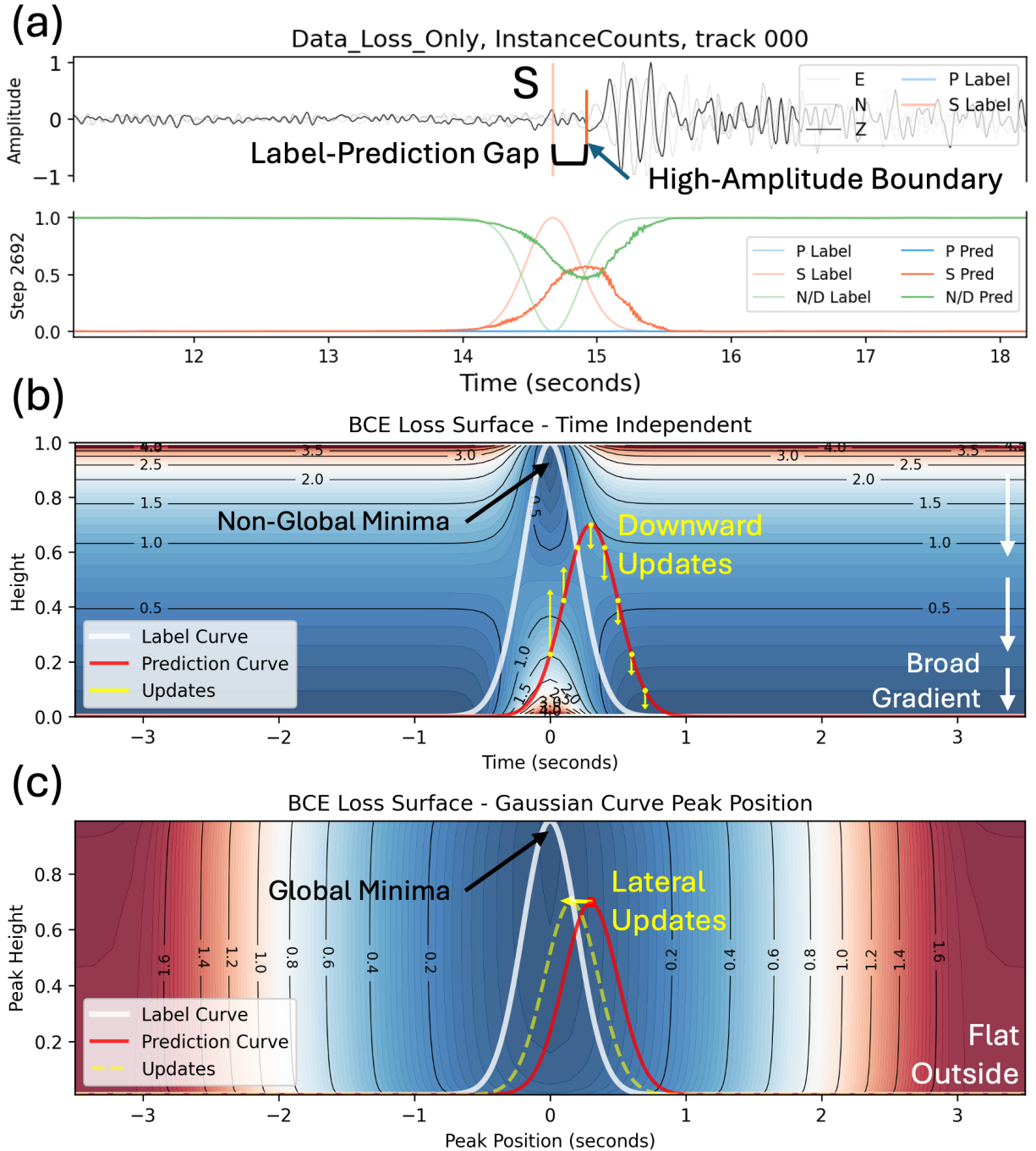
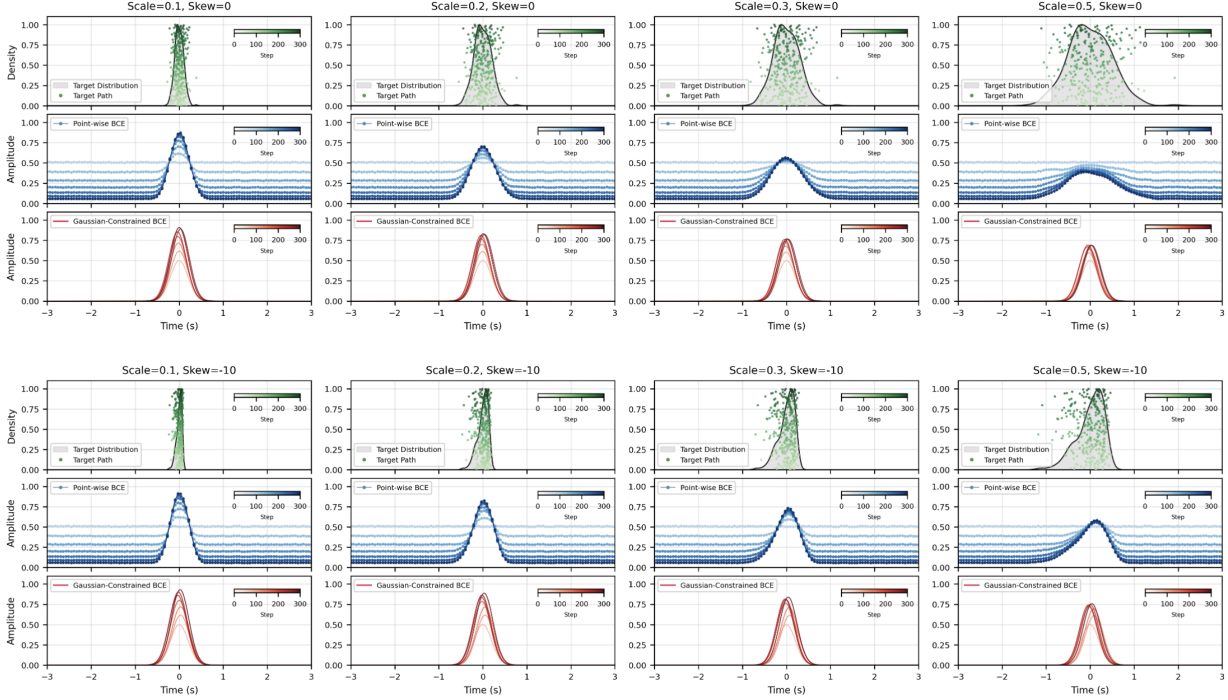


Figure 4: **The optimization trap: Actual appearance, geometric origin, and conceptual solution.** This figure reveals the geometric nature of amplitude suppression. (a) Magnified view of a suppressed S-phase prediction at step 2692, showing characteristic flattened-top appearance. (b) Theoretical loss landscape of point-wise BCE loss: low-loss region at label peak is a non-global minimum due to additional low-loss regions on both sides when amplitude is near zero. (c) Loss landscape after applying holistic shape constraint: two-sided low-loss regions vanish, leaving a single global minimum providing strong lateral guidance absent in point-wise loss.



**Figure 5: Numerical simulation: Deconstructing the key factors of the dynamic optimization trap.** This experiment removes the neural network so optimizer updates directly reflect on prediction curves. The  $2 \times 4$  grid varies distribution width ( $\sigma = 0.1, 0.2, 0.3, 0.5$ , columns) representing temporal uncertainty and skewness (0 vs. -10, rows) representing systematic bias. Each subplot shows three panels: green (target distribution with sampling path), blue (point-wise optimizer), red (Gaussian-constrained optimizer). Results demonstrate temporal uncertainty controls amplitude suppression, wider distributions yield lower amplitudes. Systematic bias introduces temporal offset only when combined with high uncertainty. The point-wise optimizer’s bottom-right profile closely resembles observed suppression (Fig. 2b), confirming this simulation captures the trap’s core mechanism.

## 2.4 Implementation: Breaking Suppression with the Shape-then-Align Framework

To realize the conceptual reshaping of the loss landscape, we implemented a cGAN-based generative framework [Mirza and Osindero, 2014]. The statistical distribution for our framework (Fig. 3b) demonstrates the complete elimination of the suppression band at 0.5 amplitude, successfully elevating the vast majority of temporally accurate predictions above the detection threshold. This systemic improvement is validated in individual cases: on the same representative event, the model trained with our framework (Fig. 2c) overcomes both symptoms of suppression, with the prediction peak confidently exceeding the 0.7 detection threshold and its temporal location correctly calibrated within the accurate range of the labeled onset, overcoming the pull of the high-amplitude boundary. This quantitative leap results in a 64% increase in the number of effective S-phase detections compared to the conventional method, confirming that by resolving the geometric flaws in the training objective, we effectively break the suppression cycle.

## 3 Discussion

We diagnose amplitude suppression as a geometric optimization trap rooted in S-wave physics. This trap originates from the physical nature of the temporal gap between the subtle S-wave onset and its subsequent high-amplitude boundary (Fig. 4a). This gap is not a fixed offset; it systematically increases with epicentral distance, becoming a highly divergent variable in any realistic dataset. This physical divergence is further compounded by inconsistencies in manual labeling, as the subtle onset is inherently difficult to pick on complex, distant waveforms (Supplementary Fig. 1). The core challenge is thus the extreme temporal uncertainty created by this combination of physical and human factors.

The CNN’s interaction with this highly uncertain gap is explained by our shared-template hypothesis. The process begins with the CNN encoder’s natural attraction to the prominent high-amplitude boundary. This occurs because the model first develops a unified template for both P and S phases based on their common opposition to the noise (Fig. 1).

By anchoring its predictions to the boundary, this template makes the physical gap manifest as a large and systematic positional error for the S-phase. As established in our results (Fig. 4, 5), the optimization process is unable to correct this error. Lacking the lateral guiding forces needed to bridge the gap.

Our hybrid objective creates an emergent lateral corrective force through a dynamic interplay of opposing pressures. The pointwise BCE loss applies its standard vertical corrective forces (Fig. 4b), attempting to pull each prediction point towards the target. Simultaneously, the discriminator applies a powerful counter-force to maintain the rigid Gaussian shape. By resisting vertical deformation, this shape constraint ensures the prediction moves as a single unit, critically preserving the single peak that defines the arrival time. This holistic structure is what channels the collective pointwise errors from BCE into a single, net lateral gradient (Fig. 4c). This emergent gradient then guides the entire rigid prediction to shift horizontally, a capability that BCE alone completely lacks.

The discriminator functions as an adaptive critic rather than fixed template, autonomously learning diverse geometries from Gaussian curves to complex boxcar functions. The tapered boxcar training provides direct evidence (Supplementary Fig. 4, Movie 3): predictions stretch and contract as the generator explores fitting its learned template to the elongated target, probing different geometric configurations before converging. This reveals an intriguing parallel to human cognitive processes: the discriminator learns abstract shape templates that the generator attempts to apply across diverse data, resembling how we mentally cycle through conceptual schemas when testing candidate interpretations against observations.

The key insight that shape must stabilize before temporal alignment can succeed is what inspired our decoupling strategy. Our discriminator-enforced approach was developed to embody this principle, allowing shape to converge independently of position. This sequence addresses a core optimization challenge, as large loss fluctuations can prevent a model from learning fine-grained features (Supplementary Fig. 7e). By first locking in the shape, we create a stable training environment where the subtle task of temporal alignment can subsequently succeed. The training dynamics confirm this insight is correct (Supplementary Fig. 3c); we observe that predictions maintain perfect geometric form while drifting temporally, and that after model resets, temporal alignment only begins again once the shape has reconverged (Supplementary Movie 3).

The framework (Supplementary Fig. 8) coordinates two loss functions with complementary roles: BCE controls temporal positioning while GAN governs geometric shape. Their dominance shifts across training (Supplementary Fig. 7e). Initially, steep BCE gradients anchor predictions temporally through instance-wise pairing [Sun et al., 2020], preventing unbounded drift and mode collapse. As BCE gradients flatten, GAN takes over to enforce shape constraints that liberate amplitude from the suppression trap. The hyperparameter  $\lambda$  balances temporal stability versus shape calibration freedom. Crucially, the handover is bidirectional. When GAN training becomes unstable with jagged predictions (Supplementary Movie 2), BCE reasserts control as a safety net, pulling predictions back until shape reconverges.

While these insights reveal broad applicability, the practical implementation involves computational trade-offs: approximately three times the training time of conventional methods (48 vs. 16 minutes for 10,000 steps) and sensitivity to hyperparameter  $\lambda$  requiring continuous monitoring. The foundational cGAN architecture presents technical challenges including training instability and mode collapse, detailed in Supplementary Notes 4.6. These risks are mitigated through the hybrid loss structure, though all protections critically depend on appropriate  $\lambda$  tuning.

Looking forward, more stable GAN variants with improved regularization [Huang et al., 2025] could enhance robustness and reduce hyperparameter sensitivity. This diagnostic insight suggests a potential parallel in image segmentation, where small structures adjacent to dominant objects might similarly escape detection if pointwise optimization lacks lateral corrective forces. Ultimately, this work transforms previously unexplained amplitude suppression into a diagnosed geometric trap with a principled solution. By revealing that pointwise optimization fundamentally lacks lateral guidance for precise localization, we provide both a diagnostic lens for recognizing similar challenges and a generalizable framework that autonomously discovers target geometry without a priori assumptions.

## 4 Methods

### 4.1 Dataset and Preprocessing

This study utilizes the INSTANCE dataset [Michellini et al., 2021], which was specifically compiled for machine learning applications. It contains a vast number of unfiltered, noisy seismic records and faithfully represents real-world complexities, including missing labels and picking errors. We deliberately selected this dataset because its inherent imperfections provide a stringent evaluation environment, essential for exposing the training bottlenecks of conventional methods and highlighting the superior robustness of our proposed approach. Following the standards of SeisBench [Woollam et al., 2022], the dataset was partitioned into a "train" set (699,980 samples), a "dev" set (115,027 samples),

and a "test" set (244,242 samples). To facilitate observation of training dynamics, we created a "track" subset from the first 100 samples of the "dev" set to visualize model predictions at each training step.

All waveform data were resampled to 100 Hz. The preprocessing workflow, adapted from Pick-Benchmark Münchmeyer et al. [2022], uses a stratified sampling scheme to balance signal and noise: two-thirds of samples contain phase arrivals (created by extracting 60-second segments centered on P- or S-wave arrivals, from which 30.01-second windows containing the arrival are randomly sampled), while one-third are pure noise samples (30.01-second windows randomly sampled from entire recordings). The labels for P- and S-phases were generated as truncated Gaussian distribution curves with a standard deviation of 0.2 seconds. The noise label was defined as (1 - phase labels). Finally, all waveforms and their corresponding labels were demeaned, detrended, and normalized.

For the experiment presented in Supplementary Figure 4 designed to test the framework’s capability as a general shape learner, we replaced the standard Gaussian labels with a more complex, tapered boxcar function. This label was generated to start at the P-wave arrival time and end at a dynamic time point calculated as  $S + (S - P) \times 1.7$ , simulating a signal duration dependent on epicentral distance. The edges of this boxcar were tapered with Gaussian functions identical in width ( $\sigma = 20$ ) to the original labels.

## 4.2 Model Architecture

Our generative framework is based on a conditional Generative Adversarial Network (cGAN) architecture Mirza and Osindero [2014], comprising a generator and a discriminator (Supplementary Fig. 8).

**Generator (G):** The generator is fulfilled by a standard PhaseNet model [Zhu and Beroza, 2018], based on the U-Net architecture [Ronneberger et al., 2015]. We utilized the unmodified implementation of PhaseNet available in SeisBench v0.9.1 [Woollam et al., 2022]. Its encoder-decoder structure with skip connections transforms seismic waveforms into corresponding label sequences. In our shape-then-align framework, the generator learns to produce geometrically coherent predictions under the guidance of both the discriminator’s holistic shape constraint and the BCE loss’s temporal anchoring.

**Discriminator (D):** We designed a lightweight convolutional neural network (CNN) as the discriminator, named BlueDisc. Its function is to distinguish whether an input label is real (from the dataset) or fake (produced by the generator), conditioned on the corresponding seismic waveform. By learning to recognize authentic label geometry, the discriminator provides holistic shape constraints that guide the generator toward producing valid Gaussian curves. The waveform and label are concatenated along the channel dimension to form the input. The network’s architecture consists of three sequential CNN blocks, where each block comprises a 1D convolutional layer followed by Batch Normalization and a LeakyReLU activation function. These blocks feed into a final fully connected layer that outputs a single logit representing the authenticity of the label. The specific parameters for each layer are detailed in Supplementary Fig. 8.

## 4.3 Training Objective

The training process of our framework is a minimax game between the generator and the discriminator. The underlying conditional adversarial loss  $\mathcal{L}_{cGAN}(\theta, \psi)$  can be expressed in the generalized form of an  $f$ -divergence [Nowozin et al., 2016]:

$$\begin{aligned} \mathcal{L}_{cGAN}(\theta, \psi) = & \mathbb{E}_{(x) \sim p_D}[f(D_\psi(G_\theta(x), x))] \\ & + \mathbb{E}_{(x,y) \sim p_D}[f(-D_\psi(y, x))] \end{aligned}$$

Here,  $\theta$  and  $\psi$  are the parameters of G and D, respectively.  $f$  is the generating function for the  $f$ -divergence. In the standard GAN setting [Goodfellow et al., 2014],  $f = -\log(1 + e^{-t})$ , which makes the objective equivalent to the original minimax objective.

To ensure the generator’s output is not only realistic but also accurately corresponds to the input condition, we follow the approach of pix2pix [Isola et al., 2016] by incorporating a conventional data-fidelity loss term alongside the adversarial loss. In our framework, the Binary Cross-Entropy loss  $\mathcal{L}_{BCE}$  from the original phase-picking task serves the same role as the  $L_1$  loss in pix2pix, providing temporal anchoring by enforcing instance-wise pairing between each input waveform and its specific ground-truth label:

$$\mathcal{L}_{BCE}(y, \hat{y}) = -\frac{1}{N} \sum_{i=1}^N [y_i \log(\hat{y}_i) + (1 - y_i) \log(1 - \hat{y}_i)]$$

where  $y_i$  and  $\hat{y}_i$  are the ground-truth and predicted phase labels for sample  $i$ , respectively.

The final overall objective is:

$$\mathcal{L}(\theta, \psi) = \mathcal{L}_{cGAN} + \lambda \mathcal{L}_{BCE}$$

where  $\lambda$  is a hyperparameter that balances the two loss terms. For our main experiments,  $\lambda$  was set to 4000 based on empirical tuning (Supplementary Fig. 2).

The training objective is to solve  $\min_G \max_D \mathcal{L}(\theta, \psi)$ . In practice, this objective is decomposed into separate loss functions for the discriminator and the generator, which are optimized alternately:

**Discriminator Loss  $\mathcal{L}_D(\theta, \psi)$ :** The discriminator aims to maximize its classification accuracy. Its total loss is  $\mathcal{L}_D(\theta, \psi) = \mathcal{L}_{Fake} + \mathcal{L}_{Real}$ , where:

$$\begin{aligned} \mathcal{L}_{Fake} &= \mathcal{L}_{BCELogits}[D_\psi(G_\theta(x), x), 0] \\ \mathcal{L}_{Real} &= \mathcal{L}_{BCELogits}[D_\psi(y, x), 1] \end{aligned}$$

**Generator Loss  $\mathcal{L}_G(\theta, \psi)$ :** The generator has two goals: to produce labels that can fool the discriminator (adversarial loss) and to fit the ground truth labels (data-fidelity loss). Its total loss is  $\mathcal{L}_G(\theta, \psi) = \mathcal{L}_{GAN} + \lambda \mathcal{L}_{Data}$ , where:

$$\begin{aligned} \mathcal{L}_{GAN} &= \mathcal{L}_{BCELogits}[D_\psi(G_\theta(x), x), 1] \\ \mathcal{L}_{Data} &= \mathcal{L}_{BCELogits}[G_\theta(x), y] \end{aligned}$$

$\mathcal{L}_{BCELogits}$  corresponds to the BCEWithLogitsLoss function in PyTorch. To accommodate this function, the outputs of both G and D are raw logits (i.e., without a final Sigmoid activation). The only exception is that the output of G is passed through a Sigmoid function before being fed to D to match the value range of the real labels. To prevent the weights of different loss terms from creating additional training variables by affecting the effective learning rate, we normalize the total loss for the discriminator and the generator by factors of 1/2 and  $(1/(1 + \lambda))$ , respectively.

#### 4.4 Implementation and Training Details

To ensure reproducibility, the random seed for all experiments was fixed to 42. All models were trained for 10,000 steps with a batch size of 100. Data shuffling was enabled only for the training set. The learning rate for both the generator and discriminator was set to  $1 \times 10^{-3}$ . We used the Adam optimizer [Kingma and Ba, 2014] with  $\beta_1$  set to 0.0 to remove the momentum term, which enhances the stability of adversarial training by preventing oscillations in the generator-discriminator equilibrium. All experiments were conducted on an NVIDIA GeForce RTX 3090 GPU. It is worth noting that differences in floating-point arithmetic across different GPU architectures may impact the reproducibility of GAN training dynamics [Micikevicius et al., 2017].

#### 4.5 Phase Arrival Picking and Evaluation

To transform the model’s continuous probability output into discrete arrival times, we employed a standard peak-picking procedure. First, all local maxima (peaks) were identified in the P- and S-phase probability curves. For the statistical visualization presented in Fig. 3, we used a lenient criterion to comprehensively illustrate the distribution patterns: all detected peaks with a probability value greater than 0.1 were paired with the nearest ground-truth label to plot their temporal offset against their peak amplitude. This lower threshold allows visualization of the full spectrum of model predictions, including those trapped in the suppression band.

For the final quantitative assessment of performance, however, a stricter dual-criteria definition was applied to identify effective detections. A picked arrival was classified as a true positive only if it met both high confidence (peak  $> 0.7$ ) and high temporal accuracy (temporal position within  $\pm 0.1$  seconds of the corresponding catalog label). This strict definition forms the basis for calculating the reported 64% increase in effective detections.

#### 4.6 Numerical Simulation Details

The numerical simulation (Fig. 5) was designed to isolate the core mechanisms of the dynamic optimization trap, independent of neural network complexities. The experiment involved an optimizer operating directly on the theoretical loss landscape derived from the point-wise BCE loss (Fig. 4b). The target for each optimization step was sampled from

a distribution whose properties—width (temporal uncertainty) and skewness (systematic bias)—were systematically varied. The experiment was structured as a  $2 \times 4$  grid. Each column corresponds to a different level of temporal uncertainty, represented by distribution widths ( $\sigma = 0.1, 0.2, 0.3, 0.5$ ). The two rows correspond to two bias conditions: a symmetric distribution (skewness = 0, top row) and a right-skewed distribution (skewness = -10, bottom row). The skewness value of -10 was chosen to simulate the systematic rightward bias observed in real S-wave predictions, where the model is attracted to the high-amplitude boundary. For all skewed distributions, the mean (center of mass) was calibrated to temporal offset zero, isolating the effect of asymmetry itself rather than a simple shift in central tendency. This design allowed us to deconstruct the individual and combined effects of uncertainty and bias. The optimizer used was Adam [Kingma and Ba, 2014] with parameters  $\beta_1 = 0.0$ ,  $\beta_2 = 0.9$ , and learning rate  $1 \times 10^{-2}$ .

**Author contributions** Conceptualization: C.-M.H.; Methodology: C.-M.H.; Software: C.-M.H., L.-H.C., I.-H.C.; Validation: C.-M.H., L.-H.C., I.-H.C.; Formal Analysis: C.-M.H., L.-H.C., I.-H.C.; Investigation: C.-M.H.; Resources: H.K.-C.; Visualization: C.-M.H.; Writing—Original Draft: C.-M.H.; Writing—Review & Editing: C.-M.H., A.-S.L.; Supervision: H.K.-C.

**Correspondence** and requests for materials should be addressed to Hao Kuo-Chen.

**Competing interests** The authors declare no competing interests.

**Supplementary information** Supplementary information is available for this paper, including:

Supplementary Notes 4.6: cGAN Training Challenges and Solutions

Supplementary Figures S1-S8:

- Fig. 1: Comparison of P-wave and S-wave arrival time label characteristics
- Fig. 2: Hyperparameter  $\lambda$  selection and its impact on convergence trajectories
- Fig. 3: Training dynamics across different loss configurations with convergence trajectories
- Fig. 4: Tapered boxcar function experiment for general shape learning
- Fig. 5: Case analysis across seismic events demonstrating robustness and limitations
- Fig. 6: Quantitative comparison of P- and S-wave predictions across three training methods
- Fig. 7: Generative adversarial training dynamics with discriminator performance and loss curves
- Fig. 8: Model architecture diagrams for cGAN framework, generator, and discriminator

Supplementary Movies:

- Movie 1 (10,000 steps): Training dynamics of purely adversarial model showing temporal instability with shape preservation, available at <https://youtu.be/rdnCe1mJpA8>
- Movie 2 (100,000 steps): Long-duration training demonstrating GAN instability requiring BCE stabilization, available at <https://youtu.be/tNiBvxP69uM>
- Movie 3 (8,000 steps): Tapered boxcar training showing dynamic shape adaptation, available at <https://youtu.be/DCB8SHBMJEg>

All supplementary materials provide additional experimental validation, architectural details, and visual evidence supporting the main findings.

**Data availability** The datasets used in this study are publicly available. INSTANCE dataset can be accessed at <https://www.pi.ingv.it/banche-dati/instance/>;

**Code availability** The code used in this study are publicly available. SeisBench is available at <https://github.com/seisbench/seisbench>; Pick Benchmark is available at <https://github.com/seisbench/pick-benchmark>; SeisBlue is available at <https://github.com/SeisBlue/SeisBlue>; The code to reproduce the results in this work is available at <https://github.com/SeisBlue/BlueDisc>.

## References

Weiqliang Zhu and Gregory C Beroza. PhaseNet: A deep-neural-network-based seismic arrival time picking method. *Geophysical Journal International*, 2018. ISSN 0956-540X. doi:10.1093/gji/ggy423.

- S. Mostafa Mousavi, William L. Ellsworth, Weiqiang Zhu, Lindsay Y. Chuang, and Gregory C. Beroza. Earthquake transformer—an attentive deep-learning model for simultaneous earthquake detection and phase picking. *Nature Communications*, 11(1):3952, 2020. doi:10.1038/s41467-020-17591-w.
- Wu-Yu Liao, En-Jui Lee, Dawei Mu, Po Chen, and Ruey-Juin Rau. ARRU phase picker: Attention recurrent-residual u-net for picking seismic p - and s -phase arrivals. *Seismological Research Letters*, 92(4):2410–2428, 2021. ISSN 0895-0695. doi:10.1785/0220200382.
- Yuanming Li, Dongsik Yoon, Bonhwa Ku, and Hanseok Ko. ConSeisGen: Controllable synthetic seismic waveform generation. *IEEE Geoscience and Remote Sensing Letters*, 21:1–5, 2024. ISSN 1545-598X. doi:10.1109/lgrs.2023.3338652.
- Tiantong Wang, Daniel Trugman, and Youzuo Lin. SeismoGen: Seismic waveform synthesis using GAN with application to seismic data augmentation. *Journal of Geophysical Research: Solid Earth*, 126(4), 2021. ISSN 2169-9313. doi:10.1029/2020jb020077.
- Yongsoo Park and Gregory C Beroza. Reducing the parameter dependency of phase-picking neural networks with dice loss. *The Seismic Record*, 5(1):55–63, 2025. ISSN 2694-4006. doi:10.1785/0320240028.
- Jesse Williams, Greg Beroza, John Pace, and Artemii Novoselov. Deep learning probabilistic regression for onset time determination. Technical report, Defense Technical Information Center. Technical Report at <https://apps.dtic.mil/sti/html/trecms/AD1211554/index.html> (2023).
- Mehdi Mirza and Simon Osindero. Conditional generative adversarial nets, 2014. Preprint at <https://arxiv.org/abs/1411.1784>.
- Phillip Isola, Jun-Yan Zhu, Tinghui Zhou, and Alexei A Efros. Image-to-image translation with conditional adversarial networks, 2016. Preprint at <https://arxiv.org/abs/1611.07004>.
- Ruoyu Sun, Tiantian Fang, and Alex Schwing. Towards a better global loss landscape of GANs, 2020. Preprint at <https://arxiv.org/abs/2011.04926>.
- Yiwen Huang, Aaron Gokaslan, Volodymyr Kuleshov, and James Tompkin. The GAN is dead; long live the GAN! a modern GAN baseline, 2025. Preprint at <https://arxiv.org/abs/2501.05441>.
- Alberto Michelini, Spina Cianetti, Sonja Gaviano, Carlo Giunchi, Dario Jozinović, and Valentino Lauciani. INSTANCE – the italian seismic dataset for machine learning. *Earth System Science Data*, 13(12):5509–5544, 2021. doi:10.5194/essd-13-5509-2021.
- Jack Woollam, Jannes Münchmeyer, Frederik Tilmann, Andreas Rietbrock, Dietrich Lange, Thomas Bornstein, Tobias Diehl, Carlo Giunchi, Florian Haslinger, Dario Jozinović, Alberto Michelini, Joachim Saul, and Hugo Soto. SeisBench—a toolbox for machine learning in seismology. *Seismological Research Letters*, 93(3):1695–1709, 2022. ISSN 0895-0695. doi:10.1785/0220210324.
- Jannes Münchmeyer, Jack Woollam, Andreas Rietbrock, Frederik Tilmann, Dietrich Lange, Thomas Bornstein, Tobias Diehl, Carlo Giunchi, Florian Haslinger, Dario Jozinović, Alberto Michelini, Joachim Saul, and Hugo Soto. Which picker fits my data? a quantitative evaluation of deep learning based seismic pickers. *Journal of Geophysical Research: Solid Earth*, 127(1), 2022. ISSN 2169-9313. doi:10.1029/2021jb023499.
- Olaf Ronneberger, Philipp Fischer, and Thomas Brox. U-net: Convolutional networks for biomedical image segmentation, 2015. Preprint at <https://arxiv.org/abs/1505.04597>.
- Sebastian Nowozin, Botond Cseke, and Ryota Tomioka. f-GAN: Training generative neural samplers using variational divergence minimization, 2016. Preprint at <https://arxiv.org/abs/1606.00709>.
- Ian J Goodfellow, Jean Pouget-Abadie, Mehdi Mirza, Bing Xu, David Warde-Farley, Sherjil Ozair, Aaron Courville, and Yoshua Bengio. Generative adversarial networks, 2014. Preprint at <https://arxiv.org/abs/1406.2661>.
- Diederik P Kingma and Jimmy Ba. Adam: A method for stochastic optimization, 2014. Preprint at <https://arxiv.org/abs/1412.6980>.
- Paulius Micikevicius, Sharan Narang, Jonah Alben, Gregory Diamos, Erich Elsen, David Garcia, Boris Ginsburg, Michael Houston, Oleksii Kuchaiev, Ganesh Venkatesh, and Hao Wu. Mixed precision training, 2017. Preprint at <https://arxiv.org/abs/1710.03740>.

## Supplementary Information

### Supplementary Note: cGAN Training Challenges and Solutions

The cGAN training process is challenging, primarily because it relies on maintaining a precise yet fragile dynamic equilibrium between the generator and the discriminator. The stability of this framework hinges on its hybrid loss structure, which is designed to counteract two primary failure modes: training instability and mode collapse.

#### Training Instability

The root of training instability lies in the spatially-limited nature of the discriminator's guidance. The discriminator can only provide effective corrective gradients when a prediction is relatively close to its target label (approx.  $< 3s$ ); beyond this finite operational range, the gradient signal from the GAN loss vanishes entirely (Fig. 4c). This inherent limitation makes the model particularly sensitive during early training or when processing batches with high temporal variance, as predictions can easily be pushed outside the discriminator's effective guidance range.

When this occurs, a cascading failure is triggered. With the prediction now outside the gradient-guided region, an oversized correction from the discriminator provokes an equally exaggerated counter-adjustment from the generator, creating a self-reinforcing loop of instability (Supplementary Movie 3). The prediction spirals away in rapid oscillations, leading to an irrecoverable collapse of the generator-discriminator equilibrium. In this scenario, the BCE loss component acts as the critical stabilizing force preventing unbounded divergence, but its effectiveness is entirely dependent on the weight of the hyperparameter  $\lambda$ . If  $\lambda$  is set too low, the stabilizing gradient from BCE is insufficient to halt the cascade.

#### Mode Collapse

The second major challenge is Mode Collapse, a phenomenon where the generator ceases to learn the complete data distribution and instead learns to produce only a few reliably deceptive samples that can fool the discriminator. Evidence includes repetitive predictions (Supplementary Fig. 5), pathologically diffuse distributions (Supplementary Fig. 6e,f), and an unnatural correlation between P and S phase predictions (Supplementary Fig. 3c,f). The root cause is that, in a purely adversarial setting, the discriminator only evaluates whether an output is statistically plausible, not whether it corresponds to a specific input.

The hybrid loss structure addresses this by incorporating a BCE loss component. BCE enforces instance-wise pairing, requiring that each input waveform must match its unique ground-truth label. This fundamentally alters the adversarial objective, shifting the goal from merely generating plausible outputs to generating the correct output for each specific input. However, this protection is also dependent on  $\lambda$  providing sufficient weight. In the tapered boxcar experiment, an excessively low  $\lambda$  value rendered the BCE constraint too weak to prevent the onset of mode collapse (Supplementary Movie 3).

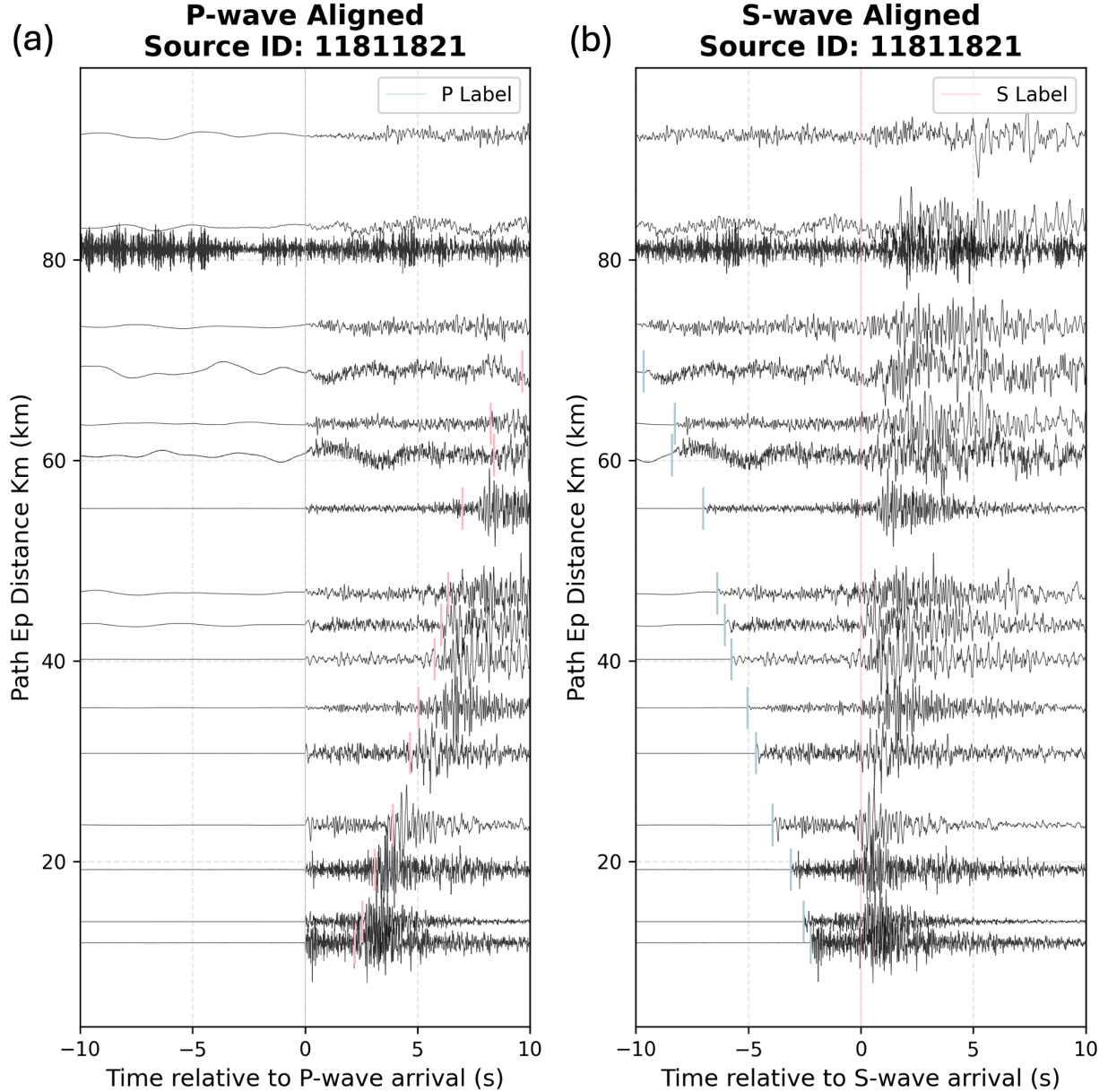


Figure 1: **Comparative Analysis of P-wave and S-wave Arrival Time Labels.** (a) P-wave: The amplitude boundary coincides with true arrival time, providing a distinct marker with low temporal uncertainty. (b) S-wave: Increasing epicentral distance causes waveform broadening and blurred amplitude boundaries. Longer propagation paths produce multiple overlapping waves, reducing amplitude gradients and annotation accuracy. This produces broad temporal uncertainty in S-wave arrivals, which combined with manual annotation errors significantly impairs model convergence.

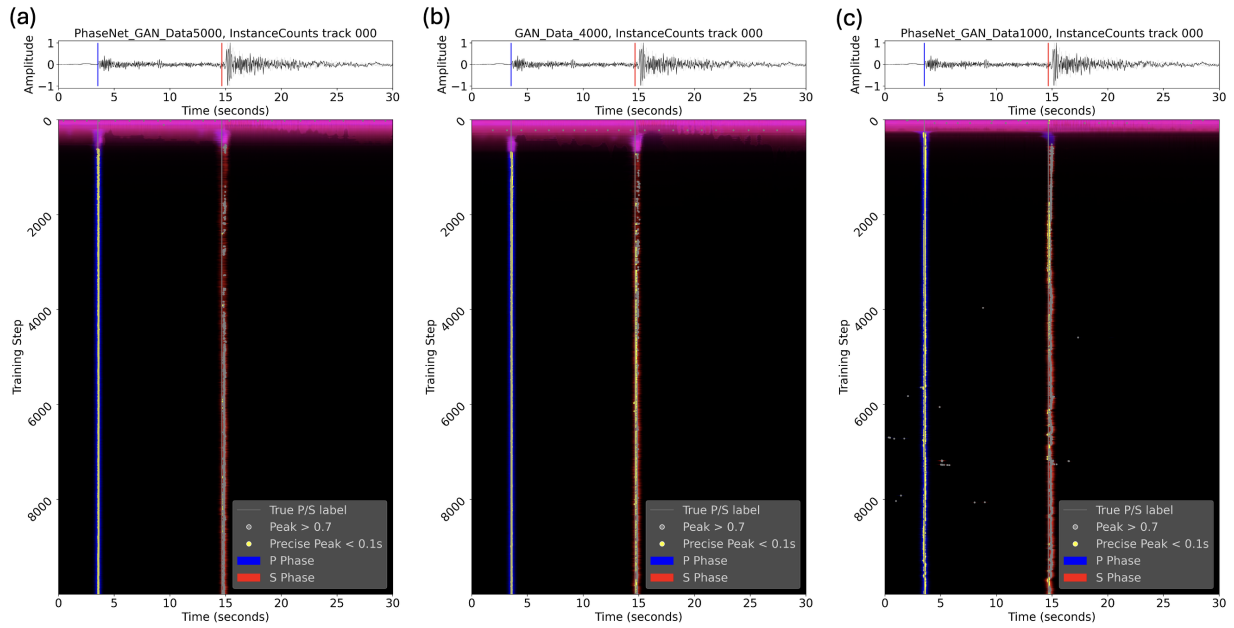
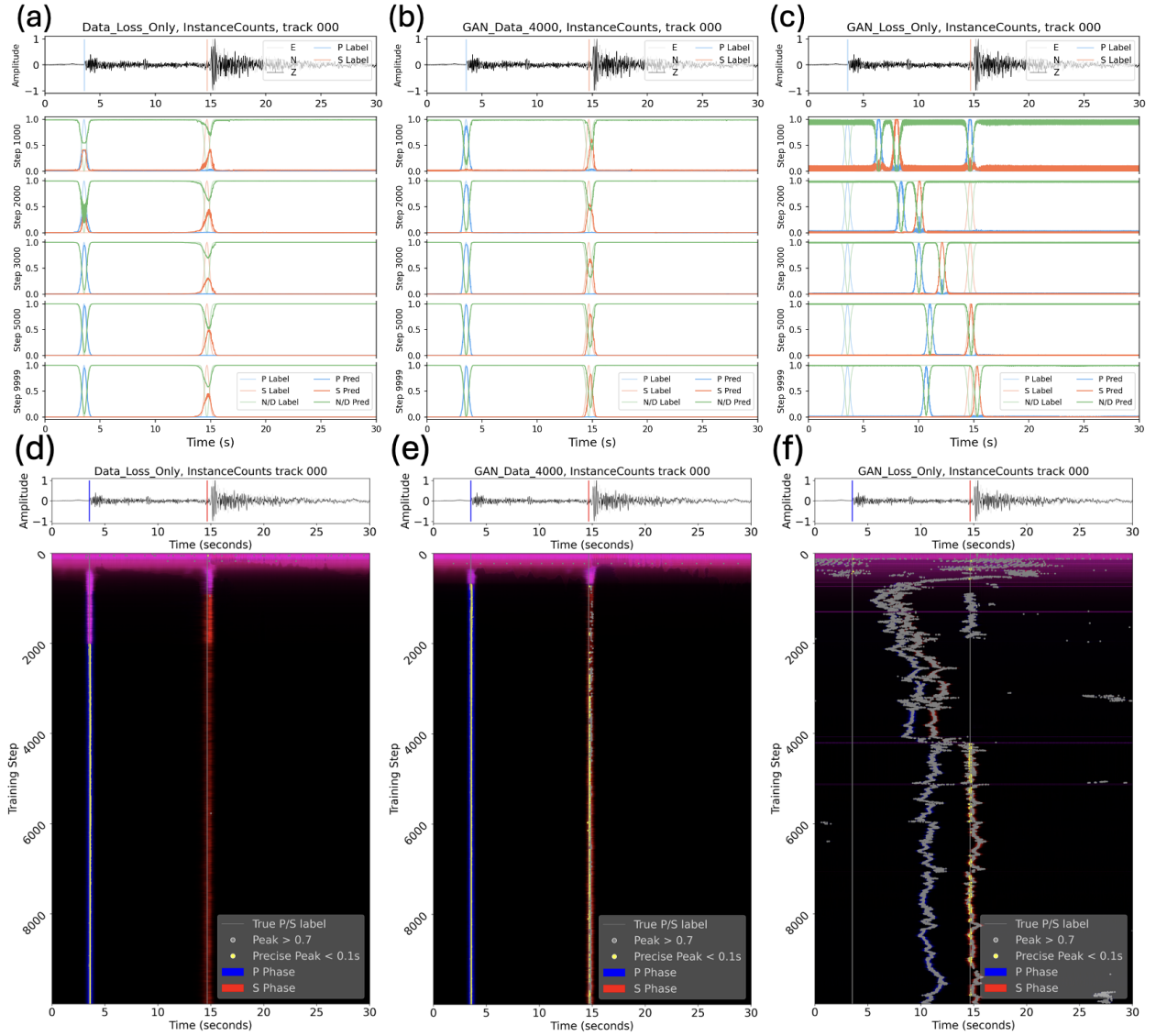


Figure 2: **The choice of hyperparameter  $\lambda$  and its impact on the convergence trajectory.** Yellow dots represent temporally accurate predictions ( $\pm 0.1$  s), gray dots fall outside this range. S-wave prediction trajectories under different  $\lambda$  settings reveal BCE-GAN loss balance: (a)  $\lambda=5000$  (too high): excessive BCE induces rightward bias, overpowering GAN's lateral correction; (b)  $\lambda=4000$  (optimal): forces reach equilibrium with stable convergence within accuracy range; (c)  $\lambda=1000$  (too low): GAN dominates but temporal localization becomes unstable. This demonstrates the critical role of  $\lambda$  in maintaining dynamic equilibrium for the shape-then-align strategy.



**Figure 3: Comparative analysis of training dynamics.** This figure compares three training methods across six panels: Data Loss only (a, d), Hybrid Loss (b, e), and GAN Loss only (c, f), showing curve evolution (top row) and peak trajectories (bottom row). Data Loss only: gradual amplitude development but eventual suppression; trajectory straight but peak never surpasses threshold. Hybrid Loss implementing shape-then-align: maintains complete geometric shape from early stages; demonstrates stable, accurate convergence. GAN Loss only: quickly grasps contour but suffers unconstrained positioning; exhibits high unstable drift. Panel (f) provides indirect mode collapse evidence: after step 4000, P-wave peak maintains relatively fixed time difference with S-wave, indicating the model learned only the decision boundary for the entire distribution rather than the complete data manifold, falling into a fixed P-S combination pattern instead of responding authentically to individual waveforms. For complete training dynamics across extended timeframes, see Supplementary Movie 1 (10,000 steps) and Movie 2 (100,000 steps).

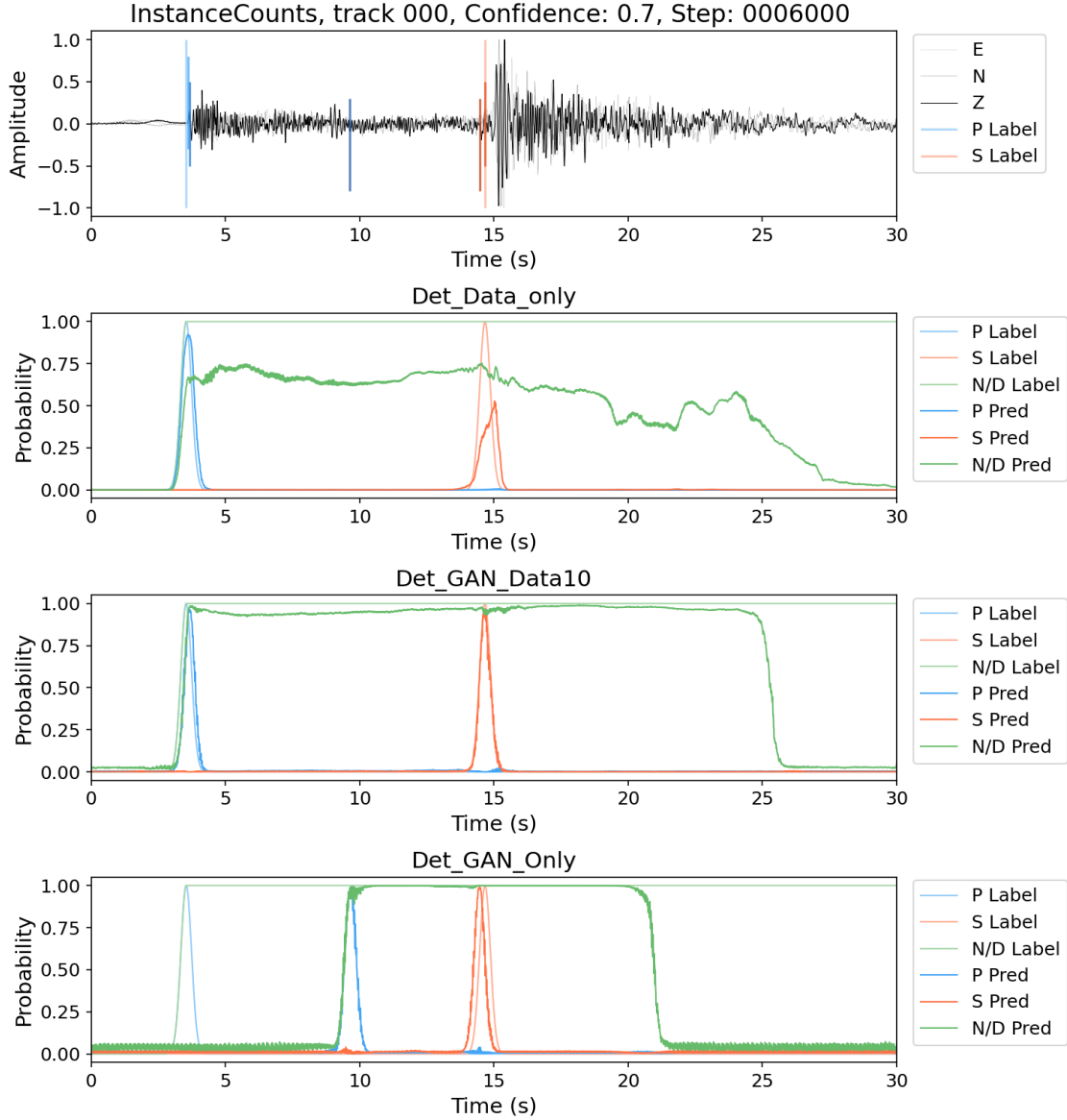
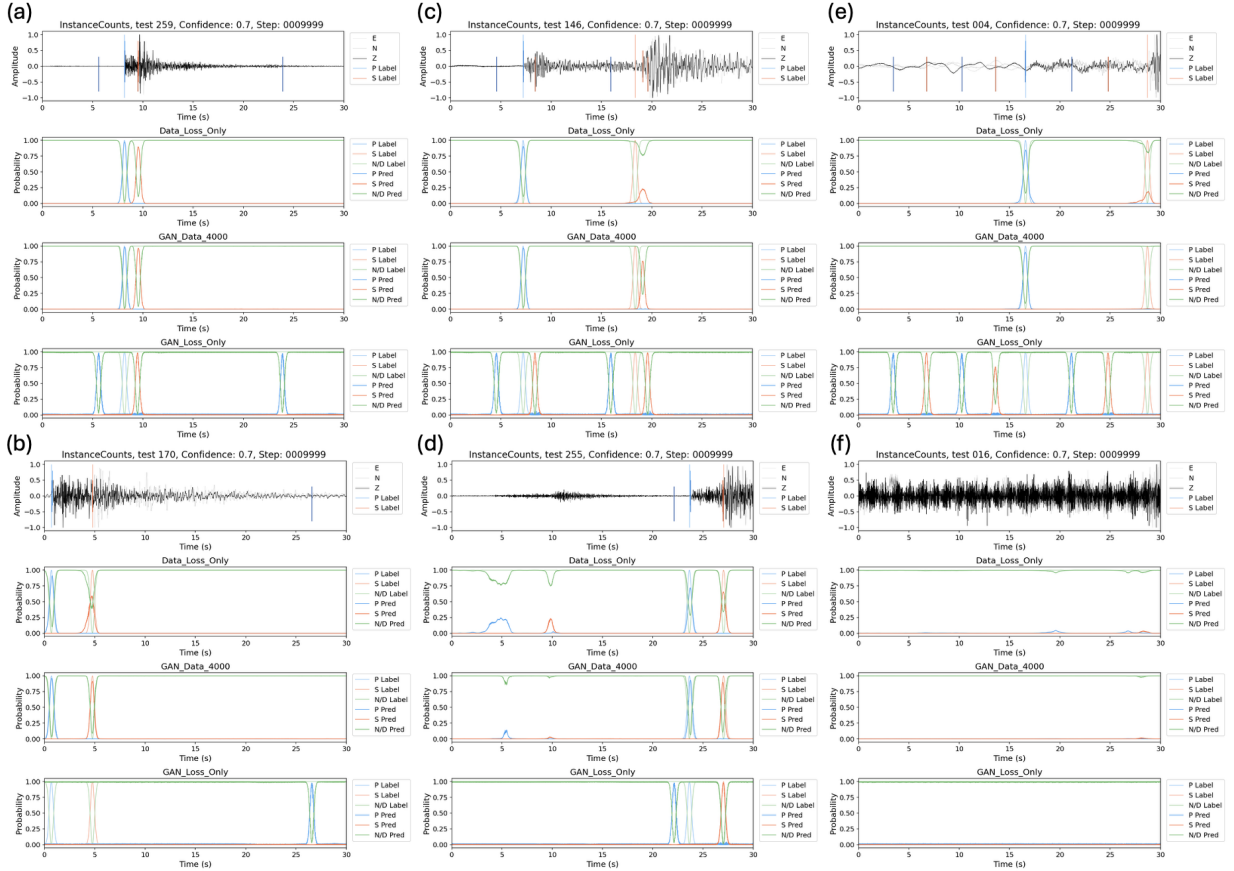
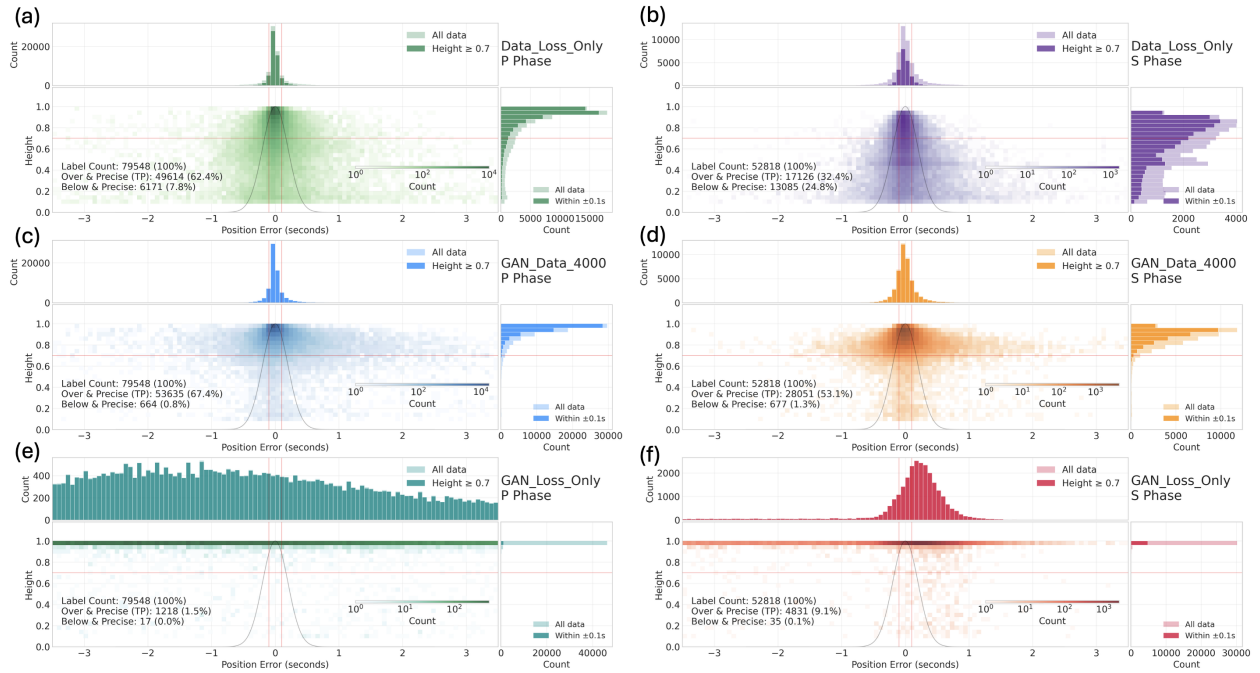


Figure 4: **Potential and challenges as a general shape learner.** To test framework generality, we replaced Gaussian labels with tapered boxcar functions (start at P-wave arrival, end at  $S + (S - P) \times 1.7$ , taper width  $\sigma = 20$ ) without changing architecture. At step 6000, the model successfully learned this non-Gaussian, dynamically-sized shape. However, this required extremely low  $\lambda = 10$ , making generator-discriminator equilibrium fragile. After step 6000, balance collapsed and the weak BCE could not stabilize training, causing irrecoverable failure. This reveals critical  $\lambda$  dependence while demonstrating the framework’s potential as a general shape learner. See Supplementary Movie 3 for complete training dynamics.



**Figure 5: Diverse case analysis: Evidence for robustness, limitations, and mode collapse.** This figure demonstrates framework performance across diverse scenarios. The hybrid loss framework shows robustness in common cases: near-field earthquakes (a, b) and pure noise (f) with correct near-zero baseline. However, limitations emerge in extreme cases: regional event (c) shows raised amplitude but miscalibrated timing; double-earthquake (d) misses the smaller signal; low-frequency noise (e) produces worse performance than conventional methods. Most critically, spanning multiple events reveals mode collapse in purely adversarial training: the GAN Loss only method generates repetitive, stereotyped predictions regardless of input waveform, highlighting the necessity of BCE as a stabilizing anchor in the hybrid loss strategy.



**Figure 6: Complete quantitative statistical comparison of P- and S-wave predictions.** Black Gaussian curves represent reference labels. This figure compares prediction peak distributions across the test set for three methods (Data Loss only, Hybrid Loss, GAN Loss only). P-wave results (a, c, e): most methods converge well, but GAN Loss only (e) shows pathological diffusion from mode collapse. S-wave results (b, d, f): Data Loss only (b) exhibits severe horizontal suppression band; GAN Loss only (f) produces high amplitudes with poor temporal accuracy; Hybrid Loss (d) successfully elevates amplitude while maintaining temporal precision. The pathological diffusion results from the generator learning only the discriminator’s decision boundary rather than the complete data manifold.

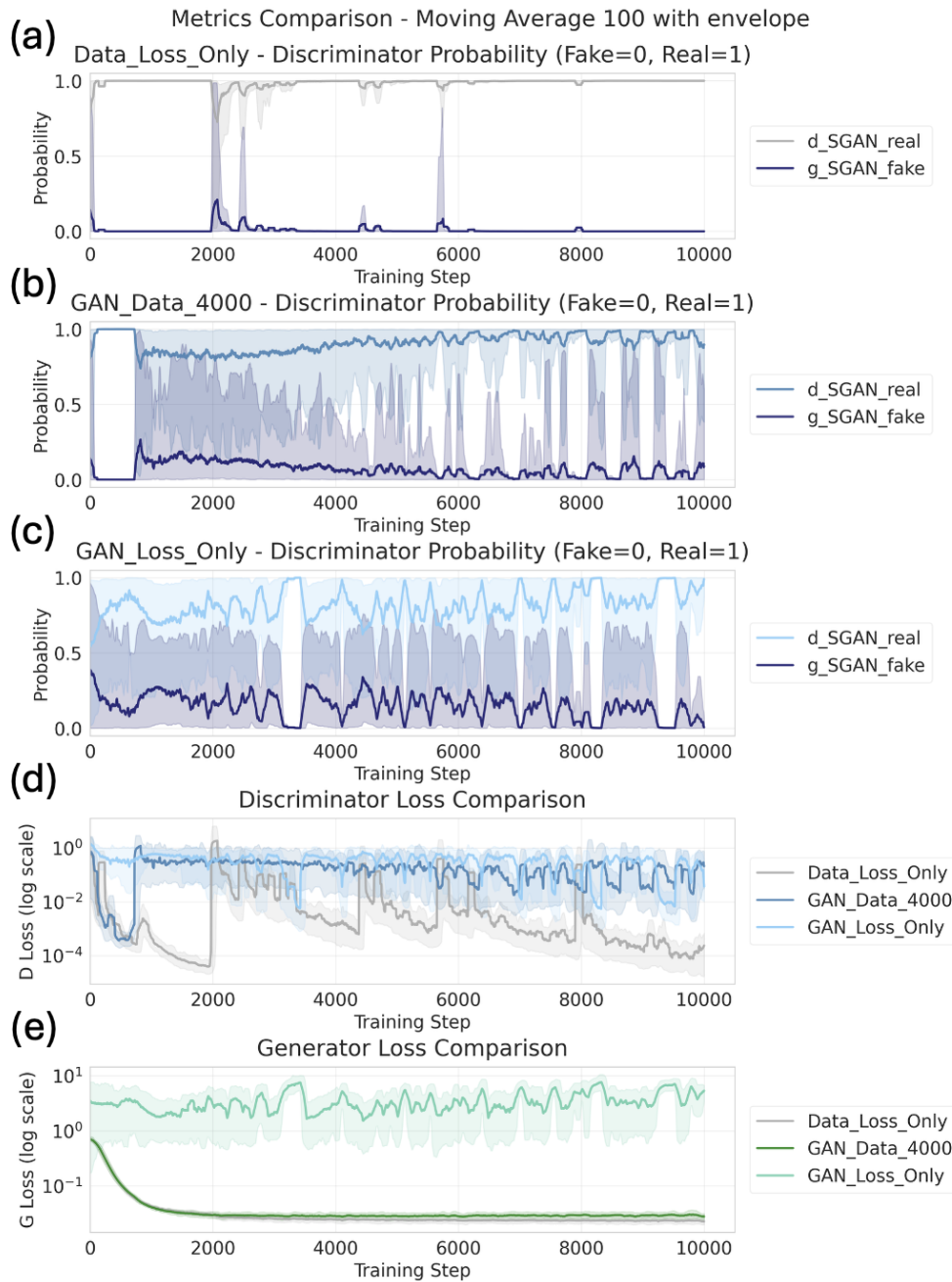


Figure 7: **Internal dynamics of generative adversarial training.** This figure reveals the continuous minimax game between generator and discriminator across five panels. Discriminator scores for real and fake labels (a, b, c) for three training methods show divergence when the discriminator successfully distinguishes labels and convergence when the generator deceives it. Discriminator loss (d) and generator loss (e) comparisons illustrate how this dynamic equilibrium drives the framework to learn label geometry.

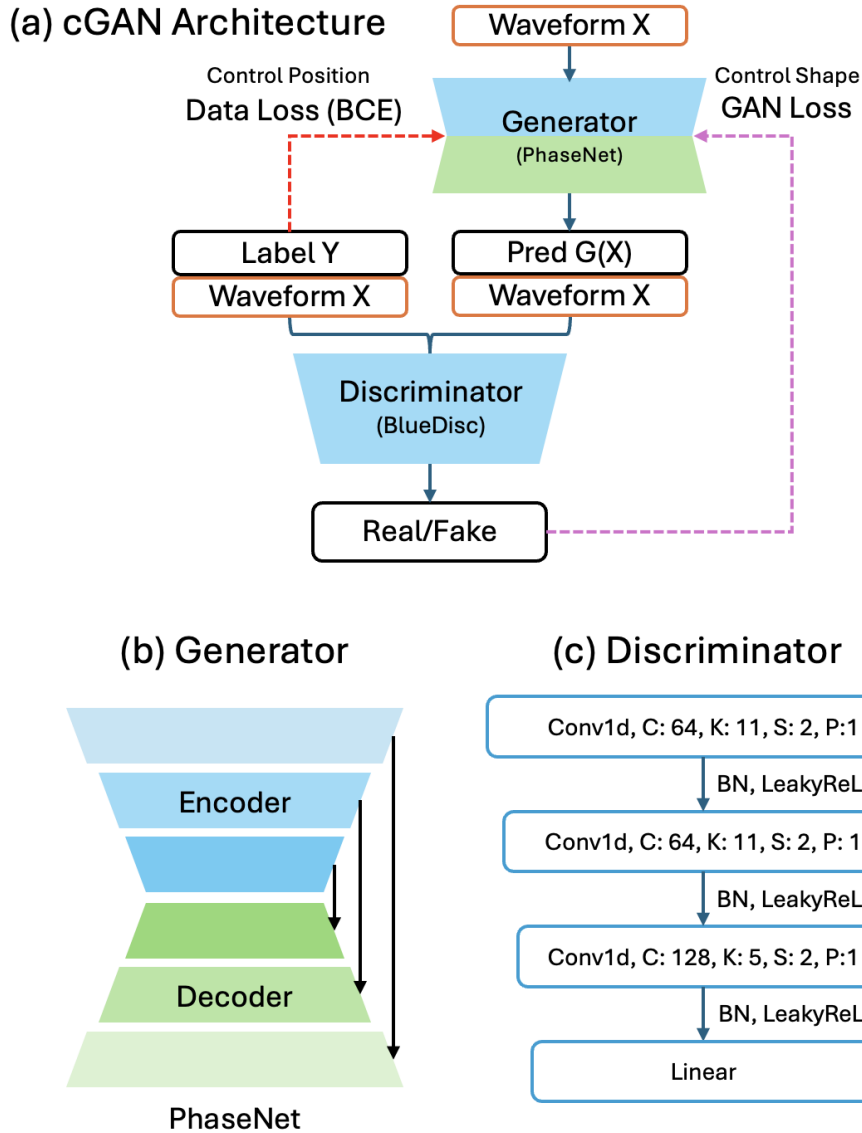


Figure 8: **Model Architecture.** (a) Complete cGAN training framework showing how the generator (G) is guided by two loss functions for task decoupling: BCE-based Data Loss controls temporal position, while GAN Loss from discriminator (D) controls shape. (b) Generator architecture: PhaseNet model based on U-Net’s encoder-decoder structure. (c) Discriminator (BlueDisc): lightweight CNN with three repeating blocks. Abbreviations: C: channel, K: kernel, S: stride, P: padding, BN: batch norm.